ADVANCING EARTH AND SPACE SCIENCES

Geophysical Research Letters

RESEARCH LETTER
10.1029/2024GL108311

Global Magnetic Reconnection During Sustained Sub-Alfvénic Solar Wind Driving

B. L. Burkholder[1,2], L.-J. Chen[2], M. Sarantos[2], D. J. Gershman[2], M. R. Argall[3], Y. Chen[4], C. Dong[4], F. D. Wilder[5], O. Le Contel[6], and H. Gurram[2,7]

[1]Goddard Planetary Heliophysics Insitute, University of Maryland Baltimore County, Baltimore, MD, USA, [2]Heliophysics Science Division, NASA Goddard Space Flight Center, Greenbelt, MD, USA, [3]Space Science Center, Institute for the Study of Earth, Oceans, and Space, University of New Hampshire, Durham, NH, USA, [4]Center for Space Physics and Department of Astronomy, Boston University, Boston, MA, USA, [5]Department of Physics, University of Texas at Arlington, Arlington, TX, USA, [6]Laboratoire de Physique des Plasmas (LPP), UMR7648, CNRS, Sorbonne Université, Université Paris-Saclay, Observatoire de Paris, Ecole Polytechnique Institut Polytechnique de Paris, Paris, France, [7]University of Maryland, College Park, MD, USA

Key Points:

- On 24 April 2023, Earth's magnetosphere experienced an interval of sustained sub-Alfvénic solar wind driving
- Sub-Alfvénic driving suppresses typical Dungey-type magnetotail reconnection but polar cap expansion is still limited
- Global simulations have strong Earthward flows localized ∼10 RE tailward of theterminator, where most new magnetospheric flux is generated

Supporting Information:

Supporting Information may be found in the online version of this article.

Correspondence to:

B. L. Burkholder,
burkbran@umbc.edu

Citation:

Burkholder, B. L., Chen, L.-J., Sarantos, M., Gershman, D. J., Argall, M. R., Chen, Y., et al. (2024). Global magnetic reconnection during sustained sub-Alfvénic Solar wind driving. *Geophysical Research Letters*, *51*, e2024GL108311. https://doi.org/10.1029/2024GL108311

Received 12 JAN 2024
Accepted 29 FEB 2024

Abstract When the solar wind speed falls below the local Alfvén speed, the magnetotail transforms into an Alfvén wing configuration. A Grid Agnostic Magnetohydrodynamics for Extended Research Applications (GAMERA) simulation of Earth's magnetosphere using solar wind parameters from the 24 April 2023 sub-Alfvénic interval is examined to reveal modifications of Dungey-type magnetotail reconnection during sustained sub-Alfvénic solar wind. The simulation shows new magnetospheric flux is generated via reconnection between polar cap field lines from the northern and southern hemisphere, similar to Dungey-type magnetotail reconnection between lobe field lines mapping to opposite hemispheres. The key feature setting the Alfvén wing reconnection apart from the typical Dungey-type is that the majority of new magnetospheric flux is added to the polar cap at local times 1–3 (21-23) in the northern (southern) hemisphere. During most of the sub-Alfvénic interval, reconnection mapping to midnight in the polar cap generates relatively little new magnetospheric flux.

Plain Language Summary Similar to how a shock wave forms around a supersonic plane, the supersonic plasma emanating from the sun forms a shock wave around Earth. However, the speed of sound through the plasma depends on different parameters that vary substantially based on the origin and evolution of solar material flowing into interplanetary space. In some coronal mass ejections, the characteristics of the plasma are such that the flow is sub-sonic, leaving the magnetosphere in a unique state. Determining whether there are any space weather impacts associated with the sub-sonic flow has been difficult due to lack of observations, but a recent event has ignited interest. This study examines the global structure and dynamics of the magnetosphere in a simulation representative of the sub-sonic flow interval of the April 2023 geomagnetic storm.

1. Introduction

Coronal mass ejections (CMEs) subject the magnetosphere to varying conditions. CMEs consist of a shock wave followed by a sheath and magnetic cloud with different plasma conditions. The CME sheath is the most geo-effective, having enhanced dynamic pressure ($P_{dyn} = \rho V_{sw}^2/2$) and interplanetary magnetic field (IMF) such that geomagnetic storms are triggered when the sheath collides with Earth. The CME magnetic cloud is also generally associated with strong IMF, meanwhile the plasma density can fall dramatically, leading to a high Alfvén speed ($V_A = B/\sqrt{\mu_0\rho}$, where B is magnetic field strength and ρ is plasma mass density). Typical solar wind velocity (V_{sw}) far exceeds the local V_A, but in many CME magnetic cloud events, V_{sw} is marginally super-Alfvénic (as defined by the Alfvén mach number $M_A \equiv V_{sw}/V_A > \sim 1$), or even sub-Alfvénic ($M_A < 1$), for a sustained interval. In fact, Hajra and Tsurutani (2022) identified 30 intervals of sustained sub-Alfvénic solar wind and the majority of events occurred within CME magnetic clouds.

During the sub-Alfvénic solar wind interaction, the magnetosphere takes on a configuration known as the Alfvén wings (Drell et al., 1965; Neubauer, 1980), which have been studied extensively with simulations. Ridley (2007) conducted magnetohydrodynamic (MHD) simulations of the magnetosphere-ionosphere system and showed that Alfvén wings exist even when $M_A > \sim 1$. They discussed that the classical view of the magnetotail has Alfvén

wings that are folded over, and the opening angle of the wings essentially determines whether there is a magnetotail. Observations and simulations presented by Nishino et al. (2022) showed asymmetric deformation of the magnetosphere during marginally super-Alfvénic driving with Parker-spiral IMF conditions. Chané et al. (2015) found the magnetosphere becomes geomagnetically quiet during sub-Alfvénic solar wind with northward IMF, implying that reconnection can be diminished to the point where it plays no significant role. Although, it was speculated that reconnection could be more strongly driven with southward IMF. Wilder et al. (2019) conducted global MHD simulations with $M_A = 1.5$ and $M_A = 4.6$, and purely northward IMF, and found that lower M_A had a lower integrated merging rate, because the blunter magnetosphere admitted less flow and magnetic flux to the merging line.

Le et al. (2000) and later Chané et al. (2015) agreed that during sub-Alfvénic solar wind driving, open flux mapping from opposite hemispheres is not forced together in the night-side, leading to a lack of magnetic shear and correspondingly weak magnetotail current sheets. Thus, during sub-Alfvénic driving, any ongoing day-side or cusp reconnection will increase the open flux content of the magnetosphere. If the sub-Alfvénic driving is sustained for long enough, it can be expected that some reconnection process will limit the growth of the polar caps. It is the purpose of this study to examine global reconnection dynamics associated with addition of new magnetospheric flux during sustained sub-Alfvénic solar wind.

2. April 2023 Coronal Mass Ejection

Figure 1 shows OMNIWeb (King & Papitashvili, 2005) data from 17:00 UT 23 April 2023 to 17:00 April 24 (time units are in hours from 00:00 April 23). A CME passed over Earth during this time, causing a geomagnetic storm with a minimum SYM-H index of −230 nT (Figure 1c), reached just after Earth exited the CME sheath and entered the magnetic cloud (see purple and orange bars, Figure 1a). After the CME sheath passed, initially, southward B_z dominated (Figure 1a). Further into the magnetic cloud, B_y increased in magnitude to −30 nT and southward B_z decreased in magnitude, eventually turning northward around 10:30 UT April 24. Both the IMF strength and solar wind velocity (Figure 1b) remained relatively constant throughout the magnetic cloud. Solar wind P_{dyn} (Figure 1c) falls dramatically during the time interval marked by vertical dashed lines. During this interval, ion density is about 0.35 cm^{-3} (not shown), with a minimum of 0.25 cm^{-3}. For comparison, minimum density on the "day the solar wind almost disappeared" (Usmanov et al., 2000) was 0.05 cm^{-3} ($M_A = 0.6$). Figure 1b shows all components of velocity are relatively steady when P_{dyn} decreases, so it is the density depletion which leads to small P_{dyn}.

The interval between vertical dashed bars is 2 hr sustained $M_A < 1$ (Figure 1d). This is significantly longer than all of the events identified by Hajra and Tsurutani (2022), but similar to some event studies (Chané et al., 2015; Lugaz et al., 2016). This sustained sub-Alfvénic solar wind driving is longer than most convection and sub-storm time-scales (Meng & Liou, 2004). Figure 1a shows that during the sub-Alfvénic interval, the IMF is B_y dominated with northward B_z. Thus, the majority of ongoing reconnection associated with new open flux is occurring near the cusps.

3. Global MHD Simulation

3.1. Simulation Description

A three-dimensional global magnetosphere simulation was performed with Grid Agnostic for MHD Extended Research Applications (GAMERA). Details of the numerical methods can be found in Zhang et al. (2019), and Sorathia et al. (2020) was first to use the solvers in a magnetospheric context. The simulation integrates the equations of ideal MHD driven by time-dependent solar wind parameters reported by OMNIWeb, given in Figure 1, which were transformed into Solar Magnetospheric (SM) coordinates for use by GAMERA. SM coordinates have the z-axis parallel to Earth's dipole axis and y-axis perpendicular to the Earth-Sun line. Variations in IMF B_x are approximated by a multiple linear regression fit of B_x to B_y and B_z (cyan line in Figure 1a). The grid extends from 100 R_E upwind of the subsolar point to 300 R_E down the magnetotail, and highest resolution is ∼0.2 R_E near the central plasma sheet. The spherical inner boundary at 2 R_E is coupled to an ionospheric model, the RE-developed Magnetosphere-Ionosphere Coupler/Solver (REMIX), a rewrite of the MIX code (Merkin & Lyon, 2010). GAMERA-REMIX is part of the Multiscale Atmosphere-Geospace Environment (MAGE) model developed by the NASA DRIVE Science Center for Geospace Storms.

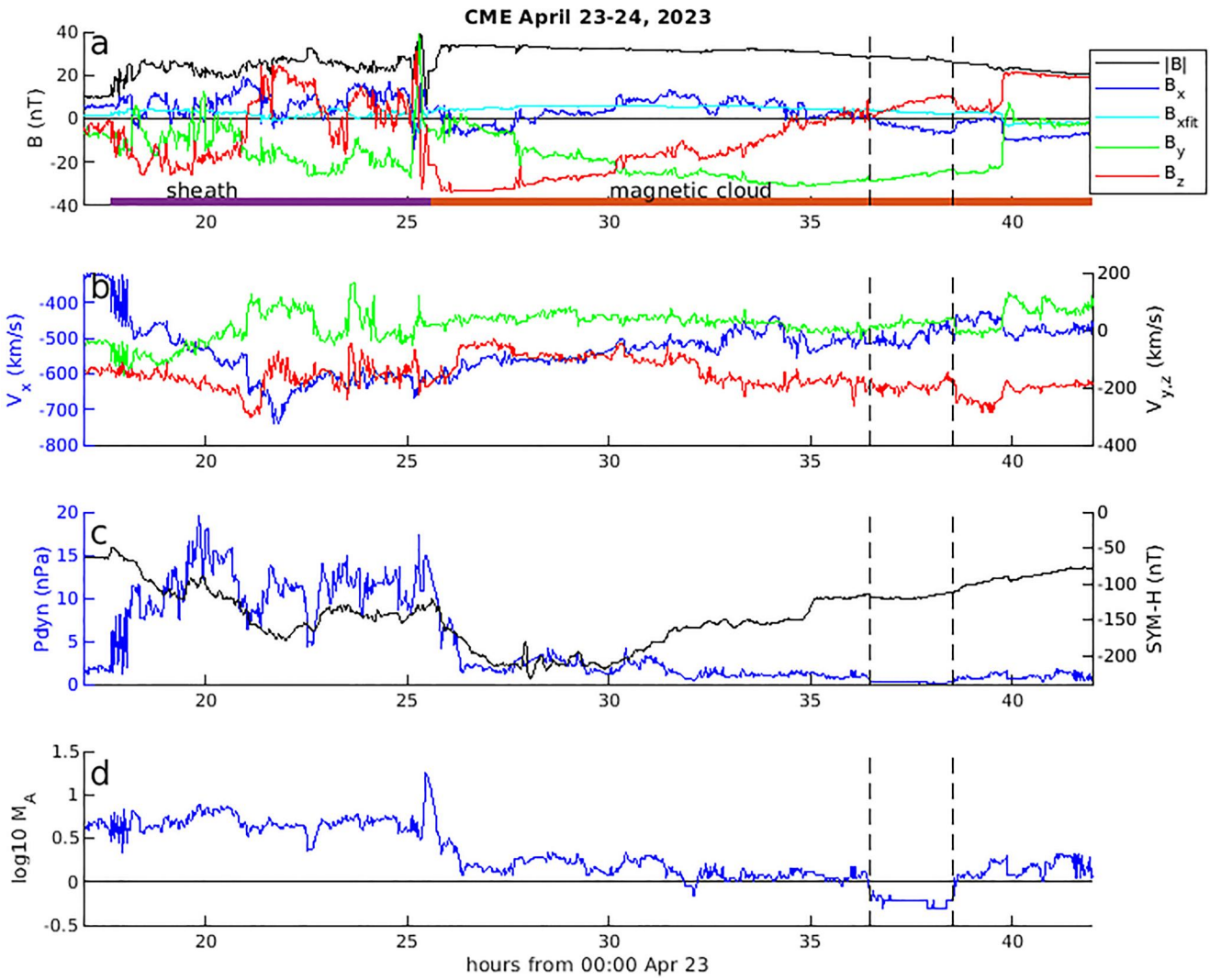

Figure 1. (a) Magnetic field, (b) plasma velocity (v_x: left side blue axis, $v_{y,z}$: right side black axis), (c) dynamic pressure (left side blue axis) and SYM-H index (right side black axis), (d) Alfvén mach number (M_A, log scale). Quantities were reported by OMNIWeb during the CME passage on April 23-24, 2023. Vector quantities were transformed into SM coordinates for the simulation (component colors are the same in (a) and (b)). The CME sheath (purple) and magnetic cloud (orange) intervals are marked in (a). Vertical dashed lines mark the boundaries of $M_A < 1$. B_{xfit} is described in the text. Only the interval surrounding the sub-Alfvénic solar wind (10:00-15:30 UT) was simulated.

Transitioning from super-to sub-Alfvénic solar wind creates computational challenges, so a few simplifications were implemented in this study. The simulation covers 10:00-15:30 UT Apr 24, which only includes <3 hr preconditioning before the sub-Alfvénic interval, rather than the entire storm driving. This minimizes the number of times the bow shock interacts with the upstream boundary. Furthermore, no coupling to the inner magnetospheric ring current module was included, which would have the effect of giving a more realistic magnetopause standoff distance (Dredger et al., 2023; Pembroke et al., 2012). Due to these limitations, the simulation should be considered as inspired by the April 2023 geomagnetic storm but not actually representative of the full storm-time dynamics. This is sufficient because the motivation is to understand global magnetic flux dynamics during sustained sub-Alfvénic solar wind driving. Note, because the simulation starts during a marginally sub-Alfvénic solar wind, it is unavoidable that the bow shock will interact with the upstream boundary during the transition to sub-Alfvénic driving. To minimize unphysical simulation results associated with this interaction, the standard methodology is to move the upstream boundary far from the magnetospheric obstacle (Chané et al., 2015; Ridley, 2007; Wilder et al., 2019). Thus, simulations in this study have the upstream boundary at 100 R_E, and it has been tested that conclusions are insensitive to a farther boundary.

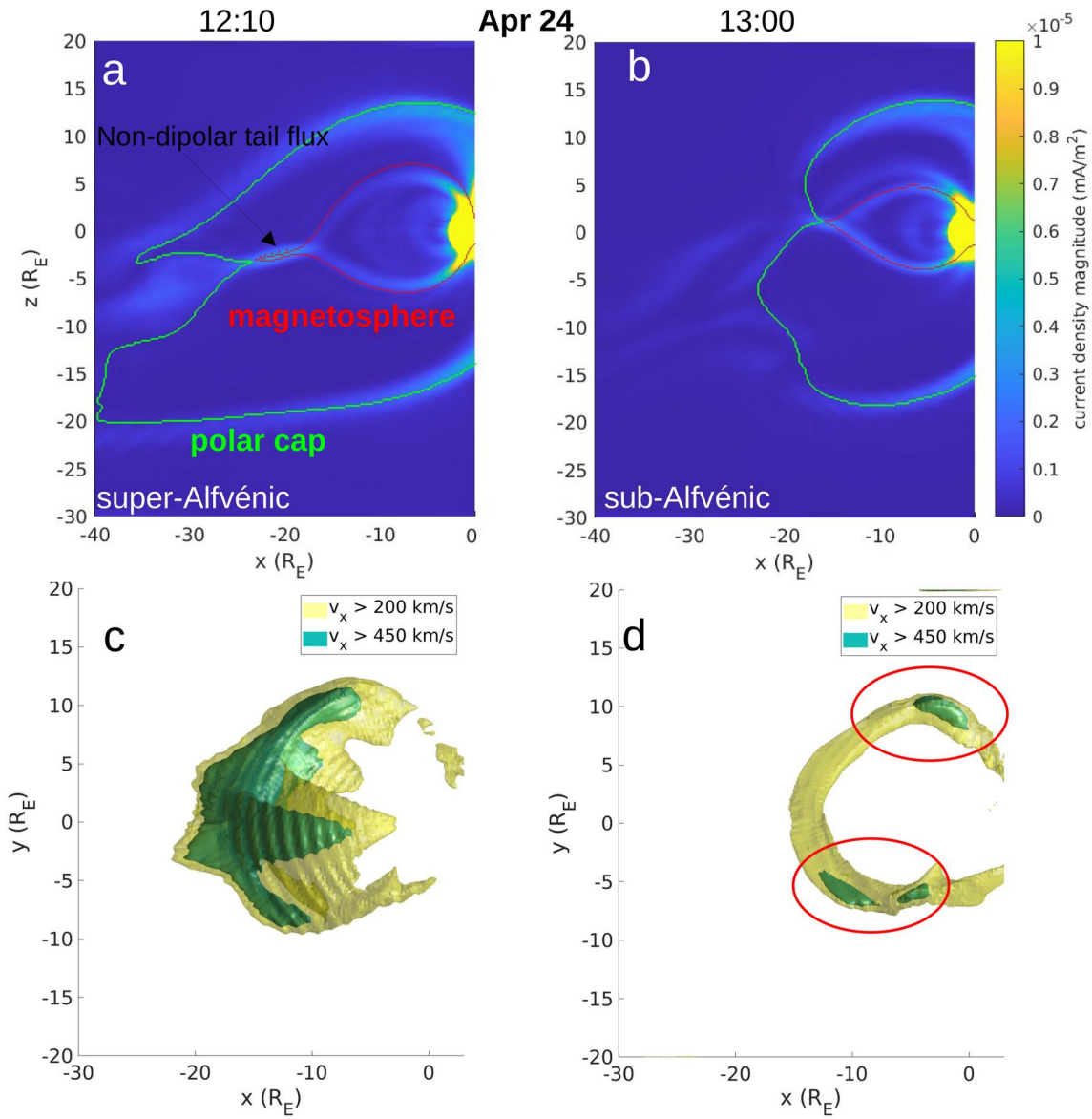

Figure 2. (a)–(b) Current density magnitude and contours of magnetic connectivity during marginally super-Alfvénic (a) and sub-Alfvénic (b) solar wind (simulation sliced at $y = 0$). The red contour outlines closed magnetospheric flux and the green contour indicates connection to the inner boundary at one end. (c)–(d) Three-dimensional earthward flow contours viewed from above the x-y plane: $v_x > 200$ km/s (yellow), $v_x > 450$ km/s (blue). Red ovals in (d) highlight fast earthward flows during sub-Alfvénic solar wind.

3.2. Simulation Results

Figures 2a and 2b show simulation current density at $y = 0$. Figure 2a is during marginally super-Alfvénic driving (t = 12:10 UT), and Figure 2b is within the sub-Alfvénic interval (t = 13:00 UT). Magnetic flux in the green contour has at least one end mapping to the inner boundary, and the red contour surrounds magnetospheric flux (both ends mapping to the inner boundary). Figure 2a shows a magnetotail current sheet with scale size of about 10 R_E (along the x-coordinate) associated with contours of stretched magnetospheric flux (labeled "non-dipolar tail flux"). During the sub-Alfvénic interval (Figure 2b), the magnetotail current sheet is <5 R_E along the x-coordinate and stretched magnetospheric flux only extends 1–2 R_E away from dipolar fields. This is expected, because during the sub-Alfvénic driving, open flux mapping from opposite hemispheres is not forced together in the night-side (Chané et al., 2015; Le et al., 2000), leading to weak magnetotail current sheets.

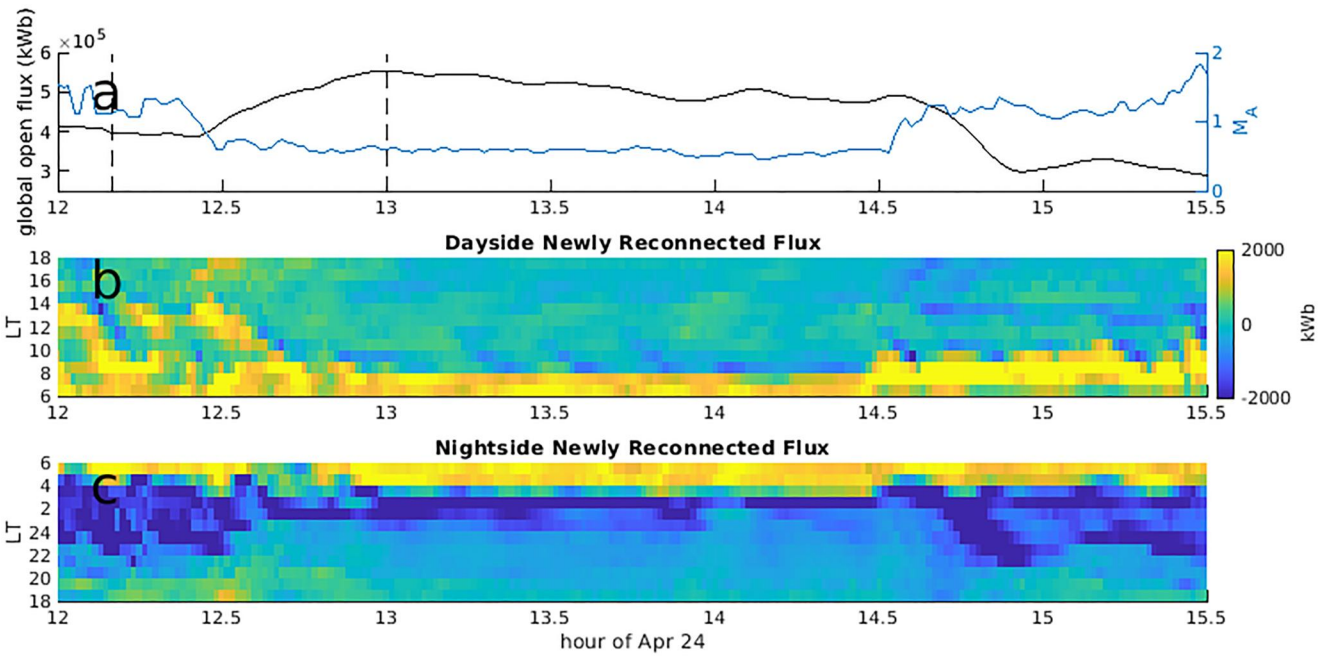

Figure 3. (a) Global open flux content ($\mathcal{O}_{pc}$, black, left axis) and Alfvén mach number (M_A, blue, right axis) surrounding the sub-Alfvénic interval. Vertical lines mark the corresponding times from Figure 2. (b) Net polar cap open flux change in 1-hr local time bins for the day-side (local time range 6–18). (c) Net open flux change for the night-side (local time range 18–24 and 0–6).

Three-dimensional flow contours in Figures 2c and 2d demonstrate that typical Dungey-type magnetotail reconnection is modified during the sub-Alfvénic interval. The contours enclose earthward flows (yellow: $v_x > 200$ km/s, blue: $v_x > 450$ km/s) for marginally super-Alfvénic (Figure 2c) and sub-Alfvénic (Figure 2d) solar wind. Tailward flows are not plotted in the three-dimensional representation due to visual interference of the magnetosheath, but reconnection is active where the flow reverses, occurring along the width of the night-side magnetosphere (from $y \sim -10\ R_E$ to $y \sim 10\ R_E$). Figure S1 in Supporting Information S1 shows cuts of v_x at $y = 0$ and $y = -6\ R_E$, depicting the strong flow reversals. The main difference in Figure 2 is that during the sub-Alfvénic interval, red circles (Figure 2d) highlight the only locations of fast earthward flows ($v_x > 450$ km/s), notably absent in the central magnetotail region (see also Figure S1 in Supporting Information S1). These fast flows will be shown to play the dominant role in generating closed magnetic flux.

The polar cap flux content ($\mathcal{O}_{pc}$) can be calculated by integrating over open flux:

$$\mathcal{O}_{pc} = r^2 \int_{open} \mathbf{B} \cdot \hat{r} \sin\theta d\phi d\theta.$$

The left-side black axis of Figure 3a shows northern hemisphere $\mathcal{O}_{pc}$ (vertical dashed lines correspond to the time-steps in Figure 2). The right-side blue axis of Figure 3a shows M_A from OMNIWeb for reference. After M_A fell below 1 just before 12:30, $\mathcal{O}_{pc}$ steadily increased until 13:00, to about 40% greater than at 12:15 (from 4×10^5 to 5.5×10^5 kWb). After 13:00 $\mathcal{O}_{pc}$ slowly decreased for ~90 min, then at 14:30 the solar wind became marginally super-Alfvénic and $\mathcal{O}_{pc}$ decreased to $\sim 3 \times 10^5$ kWb, a value slightly less than before the sub-Alfvénic interval.

Note, reconnection generating new closed magnetospheric flux will be referred to as "closing" reconnection, and new open flux is added to the polar caps via "opening" reconnection. Closing reconnection acts between two field lines mapping to the inner boundary at one end only, and opening reconnection acts between a closed magnetospheric field line and a field line with no connection to the inner boundary. Specifically during the sub-Alfvénic interval, closing reconnection acts between field lines from the two Alfvén wings, and opening reconnection produces field lines for the Alfvén wings.

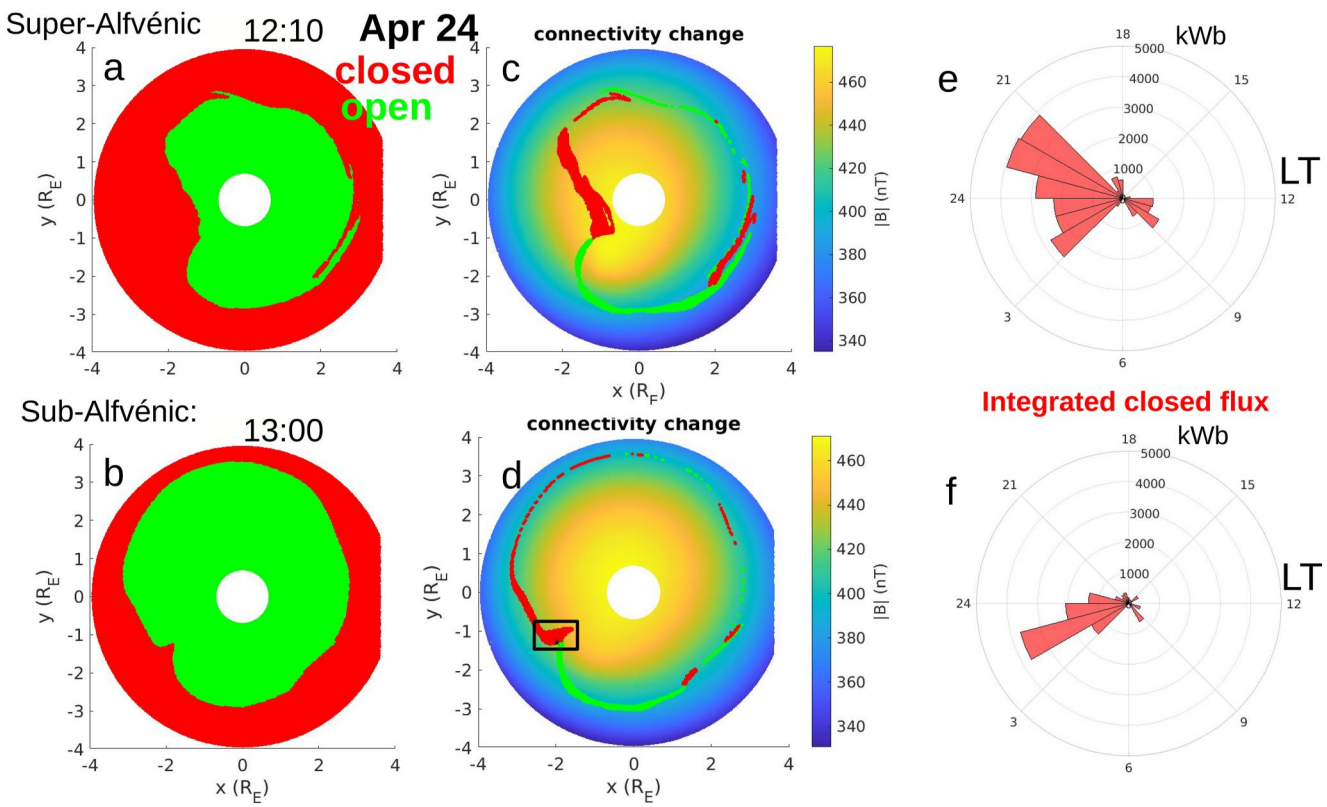

Figure 4. (a–b) Northern hemisphere magnetic connectivity maps with open (closed) flux colored green (red). Time-steps are given in the titles. (c–d) Newly reconnected magnetic fields (green and red, opened and closed, respectively) for the corresponding time-steps in the left column (see main text for description how these are calculated). The background colormap gives magnetic field strength and the black box in (d) shows where the majority of new closed flux is added during the sub-Alfvénic interval. The black star highlights the footpoint of a magnetic field line to be examined in Figure 5. (e–f) Integrated new magnetospheric flux in 1-hr local time bins.

Figures 4a and 4b show northern hemisphere magnetic connectivity during marginally super- (t = 12:10 UT) and sub-Alfvénic (t = 13:00 UT) solar wind, respectively, on a spherical grid with $r = 5\ R_E$. Green represents open polar cap and red is closed magnetospheric flux. Figures 4c and 4d show where newly reconnected flux maps into the northern hemisphere. This reconnection occurred between the simulation time in the left column (12:10, for example), and the next output 1-min later (12:11, for example). Connectivity change is determined from a fluid trace of a dense grid starting on a sphere of 5 R_E. The procedure is as follows: (a) magnetic connectivity is calculated at each point on the grid, (b) each point is pushed with the velocity field, subtracting off the field-aligned component, for 1-min (since the simulation output cadence is 1-min, a linear interpolation in time is performed on the velocity field), (c) after 1-min of tracing fluid parcels, the magnetic connectivity is calculated at their final locations. Parcels with connectivity changed from closed to open (open to closed) are colored green (red) at their starting locations. Newly reconnected flux forms a nearly continuous outline of the polar cap boundary during both super- and sub-Alfvénic solar wind (compare Figures 4a and 4b with Figures 4c and 4d). However, addition of new magnetospheric flux is comparatively localized during the sub-Alfvénic driving. This is quantified in Figures 4e and 4f, showing integrated newly closed fluxes in 1-hr local time (LT) bins. The radius of each slice gives the amount of new magnetospheric flux mapping to that LT bin in the northern polar cap. Figure 4e corresponds to marginally super-Alfvénic solar wind, where more typical Dungey-type magnetotail reconnection is occurring. Closing reconnection extends across the central magnetotail region mapping to the LT sector 21–03 in the northern polar cap. During the sub-Alfvénic interval, Figure 4f shows the majority of new magnetospheric flux maps to a single hour of LT in the northern polar cap. The black box in Figure 4d highlights this concentration of newly closed flux along the polar cap boundary, which adds the majority of new closed flux globally because it has a significant area and maps into the strong field region (see B colormap, Figure 4d).

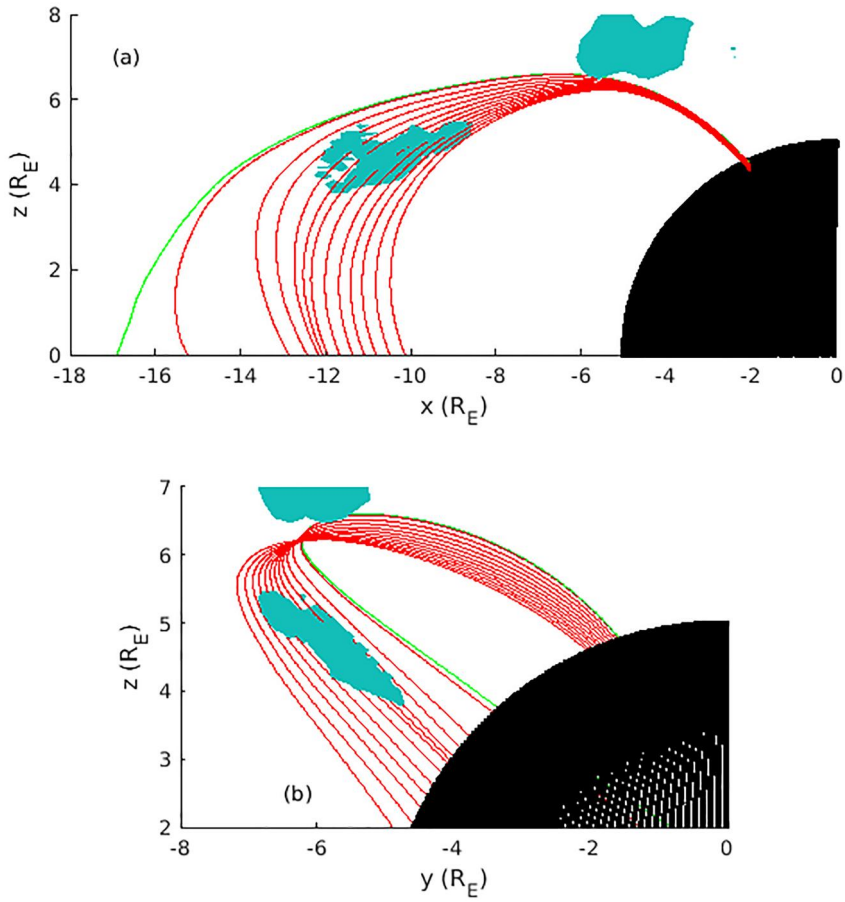

Figure 5. Red magnetic field lines (closed magnetospheric field) connect to the black starred fluid parcel in Figure 4d. The field line was drawn immediately after closing reconnection occurred (farthest left red field line in (a)) and every 5 s along the remaining 1-min fluid trajectory. The green field line (polar cap field) maps to the same fluid parcel in the northern hemisphere 1 s (1 fluid parcel push) before the reconnection occurred. The blue contour shows $v_x > 450$ km/s at the end of the 1-min fluid tracing, viewed in the x-z plane in (a) and y-z plane in (b). The grid of fluid parcels is shown at 5 R_E.

Figures 3b and 3c show the LT distribution of where newly reconnected flux maps to the northern polar cap as a function of time. Color quantifies net change of open flux, thus, yellow indicates more flux opened in that local time sector and blue more flux closed. Figure 3b shows the local time sector 6–18, where the majority of new open flux is added, and Figure 3c shows the local time sector 18–24 and 0–6, where the majority of new magnetospheric flux is added. Qualitatively, it is clear that the sub-Alfvénic interval (see M_A in Figure 3a) is different from the surrounding marginally super-Alfvénic driving. Figure 3b shows that the opening cusp reconnection mapping to the day-side polar cap is diminished in extent during the sub-Alfvénic interval, but still active. Figure 3c demonstrates new magnetospheric flux is added dominantly in the sector mapping to 2–3 LT in the northern polar cap, different from the marginally super-Alfvénic solar wind, where newly generated magnetospheric flux spreads across the night-side (LT $\sim 21 - 3$).

Figure 5 shows time history of the magnetic field line mapping to the black star fluid parcel from Figure 4d. This parcel was identified as having a newly closed magnetic connection based on the fluid tracing. Furthermore, the reconnection occurred in the region where the majority of new magnetospheric flux maps to the northern polar cap. Immediately after reconnection occurred, the fluid parcel was attached to the left-most red magnetic field line in Figure 5a. The green field line connects to the same fluid parcel 1-s before the reconnection occurred, when it was still open. The remaining red field lines are attached to the same fluid parcel drawn every 5 s along its trajectory. The noteworthy aspect of the red field lines is that they are convected through the strong earthward flow region (blue contour representing $v_x > 450$ km/s at $z = 4$–$5\ R_E$, viewed in x-z plane in 5a and y-z plane in 5b). This is the typical three-dimensional magnetic connection for those fluid parcels colored red in the black box from

Figure 4d. It can therefore be concluded that the fast flows are an indicator of where the majority of new magnetospheric flux is exhausted during the sub-Alfvénic interval. This occurs symmetrically in both hemispheres (in the dusk sector for the southern hemisphere), which is a significant modification to typical Dungey-type magnetotail reconnection. Thus, the main difference between closing reconnection during sub-Alfvénic solar wind driving and typical Dungey-type magnetotail reconnection is that the primary location is localized where new closed flux is added to the magnetosphere.

4. Summary and Conclusions

Sustained sub-Alfvénic solar wind leads to lack of a current sheet extending 10s of R_E down-tail, because the mapping of open polar cap field lines is mostly in the direction of the IMF, with little magnetic flux squeezed into a stretched magnetotail configuration. The sub-Alfvénic solar wind drives a modified Dungey cycle where reconnection producing significant closed magnetic flux does not occur uniformly across the night-side. In this event, with B_y dominant IMF, the simulation shows that reconnection adds new magnetospheric flux primarily by reconnection away from midnight local time, about 10 R_E tail-ward of the symmetric cusp opening reconnection locations (which are close to the noon-midnight terminator).

There is still an important open question of exactly how the global flux circulation is modified. Watanabe and Sofko (2008) classified polar cap convection in terms of magnetospheric field topology when the IMF is B_y dominant, but future work is needed to determine if the sub-Alfvénic solar wind needs to be taken as a special case. More generally, it is also not known how different solar wind parameters will effect the topology of closing reconnection during sub-Alfvénic solar wind driving. Furthermore, localized resistivity inspired by data mining of observed reconnection locations has been shown to suppress reconnection closer to the Earth (Arnold et al., 2023), which could be an important factor when the tail current sheet retreats toward Earth during the transition from super-to sub-Alfvénic solar wind.

The sub-Alfvénic solar wind without a strong southward IMF is not generally considered geoeffective in terms of geomagnetic indices. However, Figure 1c shows the SYM-H index is held constant for most of the sub-Alfvénic interval in this event. Thus, the ring current decay stalls during the sub-Alfvénic driving, lengthening the magnetospheric recovery time to pre-storm SYM-H levels (see Chen et al. (2024) for more discussion). Numerical simulations including ring current physics may help explain how it is held steady during the sub-Alfvénic driving.

Data Availability Statement

The global MHD simulation outputs are archived at Zenodo - doi: 10.5821/zenodo.10479736 (Burkholder, 2024).

Acknowledgments
We acknowledge use of NASA/GSFC's Space Physics Data Facility's OMNIWeb. We thank the team of the Center for Geospace Storms for providing the MAGE model. We also acknowledge the Texas Advanced Computing Center (TACC) at The University of Texas at Austin for providing HPC resources that have contributed to the research results reported within this paper. URL: http://www.tacc.utexas.edu. Funding for this work is provided by the NASA MMS Mission and MMS Early Career Grant 80NSSC22K0949. MRA was additionally funded by NASA H-GIO Grant 80NSSC22K0187.

References

Arnold, H., Sorathia, K., Stephens, G., Sitnov, M., Merkin, V. G., & Birn, J. (2023). Data mining inspired localized resistivity in global mhd simulations of the magnetosphere. *Journal of Geophysical Research: Space Physics*, *128*(2), e2022JA030990. https://doi.org/10.1029/2022JA030990

Burkholder, B. (2024). Quad resolution GAMERA global MHD: April 2023 storm, sub-alfvenic interval. *Zenodo*. https://doi.org/10.5281/zenodo.10479736

Chané, E., Raeder, J., Saur, J., Neubauer, F. M., Maynard, K. M., & Poedts, S. (2015). Simulations of the earth's magnetosphere embedded in sub-alfvénic solar wind on 24 and 25 may 2002. *Journal of Geophysical Research: Space Physics*, *120*(10), 8517–8528. https://doi.org/10.1002/2015JA021515

Chen, L.-J., Gershman, D., Burkholder, B., Chen, Y., Sarantos, M., Jian, L., et al. (2024). Earth's alfvén wings driven by the April 2023 coronal mass ejection. *arXiv e-prints*. arXiv:2402.08091.

Dredger, P. M., Lopez, R. E., & Collado-Vega, Y. M. (2023). Comparing magnetopause predictions from two mhd models during a geomagnetic storm and a quiet period. *Frontiers in Astronomy and Space Sciences*, *10*. https://doi.org/10.3389/fspas.2023.1213331

Drell, S. D., Foley, H. M., & Ruderman, M. A. (1965). Drag and propulsion of large satellites in the ionosphere: An alfvén propulsion engine in space. *Journal of Geophysical*, *70*(13), 3131–3145. https://doi.org/10.1029/JZ070i013p03131

Hajra, R., & Tsurutani, B. T. (2022). Near-earth sub-alfvénic solar winds: Interplanetary origins and geomagnetic impacts. *The Astrophysical Journal*, *926*(2), 135. https://doi.org/10.3847/1538-4357/ac4471

King, J. H., & Papitashvili, N. E. (2005). Solar wind spatial scales in and comparisons of hourly wind and ace plasma and magnetic field data. *Journal of Geophysical Research*, *110*(A2). https://doi.org/10.1029/2004JA010649

Le, G., Russell, C. T., & Petrinec, S. M. (2000). The magnetosphere on may 11, 1999, the day the solar wind almost disappeared: I. Current systems. *Geophysical Research Letters*, *27*(13), 1827–1830. https://doi.org/10.1029/1999GL010774

Lugaz, N., Farrugia, C. J., Huang, C.-L., Winslow, R. M., Spence, H. E., & Schwadron, N. A. (2016). Earth's magnetosphere and outer radiation belt under sub-Alfvénic solar wind. *Nature Communications*, *7*(1), 13001. https://doi.org/10.1038/ncomms13001

Meng, C.-I., & Liou, K. (2004). Substorm timings and timescales: A new aspect. *Space Science Reviews*, *113*(1), 41–75. https://doi.org/10.1023/B:SPAC.0000042939.88548.68

Merkin, V. G., & Lyon, J. G. (2010). Effects of the low-latitude ionospheric boundary condition on the global magnetosphere. *Journal of Geophysical Research*, *115*(A10). https://doi.org/10.1029/2010JA015461

Neubauer, F. (1980). Nonlinear standing alfvén wave current system at io: Theory. *Journal of Geophysical Research*, *85*(A3), 1171–1178. https://doi.org/10.1029/JA085iA03p01171

Nishino, M. N., Hasegawa, H., Saito, Y., Lavraud, B., Miyashita, Y., Nowada, M., et al. (2022). Asymmetric deformation of the Earth's magnetosphere under low Alfvén Mach number solar wind: Observations and MHD simulation. *Earth Planets and Space*, *74*(1), 180. https://doi.org/10.1186/s40623-022-01744-w

Pembroke, A., Toffoletto, F., Sazykin, S., Wiltberger, M., Lyon, J., Merkin, V., & Schmitt, P. (2012). Initial results from a dynamic coupled magnetosphere-ionosphere-ring current model. *Journal of Geophysical Research*, *117*(A2). https://doi.org/10.1029/2011JA016979

Ridley, A. J. (2007). Alfvén wings at earth's magnetosphere under strong interplanetary magnetic fields. *Annales Geophysicae*, *25*(2), 533–542. https://doi.org/10.5194/angeo-25-533-2007

Sorathia, K. A., Merkin, V. G., Panov, E. V., Zhang, B., Lyon, J. G., Garretson, J., et al. (2020). Ballooning-interchange instability in the near-earth plasma sheet and auroral beads: Global magnetospheric modeling at the limit of the mhd approximation. *Geophysical Research Letters*, *47*(14), e2020GL088227. https://doi.org/10.1029/2020GL088227

Usmanov, A. V., Goldstein, M. L., & Farrell, W. M. (2000). A view of the inner heliosphere during the may 10–11, 1999 low density anomaly. *Geophysical Research Letters*, *27*(23), 3765–3768. https://doi.org/10.1029/2000GL000082

Watanabe, M., & Sofko, G. J. (2008). Synthesis of various ionospheric convection patterns for imf by-dominated periods: Split crescent cells, exchange cells, and theta aurora formation. *Journal of Geophysical Research*, *113*(A9). https://doi.org/10.1029/2007JA012868

Wilder, F. D., Lopez, R. E., Eriksson, S., Pham, K., & Lin, D. (2019). The relative importance of geoeffective length versus alfvén wing formation in the saturation of the ionospheric reverse convection potential. *Geophysical Research Letters*, *46*(3), 1126–1131. https://doi.org/10.1029/2018GL080639

Zhang, B., Sorathia, K. A., Lyon, J. G., Merkin, V. G., Garretson, J. S., & Wiltberger, M. (2019). Gamera: A three-dimensional finite-volume MHD solver for non-orthogonal curvilinear geometries. *The Astrophysical Journal - Supplement Series*, *244*(1), 20. https://doi.org/10.3847/1538-4365/ab3a4c